

Effects of thermal treatment on physical and mechanical properties of Valdieri Marble - NW Italy

Original

Effects of thermal treatment on physical and mechanical properties of Valdieri Marble - NW Italy / Vagnon, F.; Colombero, C.; Colombo, F.; Comina, C.; Ferrero, A. M.; Mandrone, G.; Vinciguerra, S. C.. - In: INTERNATIONAL JOURNAL OF ROCK MECHANICS AND MINING SCIENCES. - ISSN 1365-1609. - ELETTRONICO. - 116:(2019), pp. 75-86. [10.1016/j.ijrmms.2019.03.006]

Availability:

This version is available at: 11583/2742629 since: 2019-07-17T18:46:51Z

Publisher:

Elsevier Ltd

Published

DOI:10.1016/j.ijrmms.2019.03.006

Terms of use:

This article is made available under terms and conditions as specified in the corresponding bibliographic description in the repository

Publisher copyright

Elsevier postprint/Author's Accepted Manuscript

© 2019. This manuscript version is made available under the CC-BY-NC-ND 4.0 license
<http://creativecommons.org/licenses/by-nc-nd/4.0/>. The final authenticated version is available online at:
<http://dx.doi.org/10.1016/j.ijrmms.2019.03.006>

(Article begins on next page)

1 **Effects of Thermal Treatment on Physical and Mechanical**
2 **Properties of Valdieri Marble - NW Italy**

3 Federico Vagnon, Department of Earth Sciences, Università di Torino, Torino, 10125, Italy,
4 federico.vagnon@unito.it (corresponding author)

5 Chiara Colombero, Department of Environment, Land and Infrastructure Engineering,
6 Politecnico di Torino, Torino, 10129, Italy, chiara.colombero@polito.it

7 Fabrizio Colombo, Principal consultant – Ultra Petrography & Geosciences Inc., Canada,
8 fab.petrologic@gmail.com

9 Cesare Comina, Department of Earth Sciences, Università di Torino, Torino, 10125, Italy,
10 cesare.comina@unito.it

11 Anna Maria Ferrero, Department of Earth Sciences, Università di Torino, Torino, 10125, Italy,
12 anna.ferrero@unito.it

13 Giuseppe Mandrone, Department of Earth Sciences, Università di Torino, Torino, 10125, Italy,
14 giuseppe.mandrone@unito.it

15 Sergio Carmelo Vinciguerra, Department of Earth Sciences, Università di Torino, Torino,
16 10125, Italy, sergiocarmelo.vinciguerra@unito.it

17 **Abstract**

18 The effect of high temperatures as a degrading factor of rock materials is investigated in this
19 study. Valdieri Marble samples, collected in a quarry in North-western Italian Alps, were
20 subjected to thermal cycles (ranging from 105° to 600° C) and to subsequent non-destructive
21 and destructive laboratory tests with the aim of evaluating the variation of physical and
22 mechanical properties as a function of temperature variations. Physical and mechanical
23 measurements were complemented with microscopic observations on thin sections. The
24 increase of crack density with temperature and the consequent porosity increases were found
25 to be the main causes of the degradation of physical and mechanical properties.

26 In general, density, ultrasonic pulse velocity, wet electrical resistivity, uniaxial compressive
27 strength and Young's moduli decrease as temperature increases. By contrast, peak strain and
28 porosity increase. Correlations between temperature and physical-mechanical properties were
29 proposed and compared to other relationships already established in scientific literature. A
30 damage parameter to quantify the degradation of mechanical properties with temperature is
31 also proposed.

32

33 **Keywords**

34 Valdieri Marble; thermal treatment; mechanical and physical properties; micro-cracks.

35

36 1. Introduction

37 The overall physical and mechanical behaviour of upper crustal rocks is given by the
38 combination of their geological formation and the mechanical and thermal stresses acting over
39 time [1]. While mechanical effects have been widely investigated, less attention has been spent
40 to the effect of temperature, which is a main mechanism of degradation and weakening of
41 rocks. In natural volcanic and geothermal environments, high temperature gradients induced
42 by rapid magmatic/supercritical fluid injections can induce permanent changes to the hosting
43 material, via mineralogical transition and hydrothermal alteration, eventually enhancing
44 potential flank collapses [2]. Similarly, in many rock-engineering applications, such as drilling,
45 deep petroleum boring, geothermal energy exploitation, nuclear waste disposal, CO₂ storage
46 etc., the effect of high temperatures on the mechanical properties of the materials is to be
47 considered for a safe and successful design. Last but not least, an important field in which the
48 effect of high temperatures on rocks plays a fundamental role is the maintenance/repair of
49 stone-built heritage damaged by fire [3-6].

50 Mechanically, the effect of elevated temperatures on rocks is controlled by several parameters,
51 among which grain size, porosity and strain rate are the most sensitive ones [7].

52 Two main degradation mechanisms are usually attributed to rock samples exposed to a
53 significant temperature gradient. The first one is the propagation of pre-existing cracks, or the
54 development of new ones, driven by thermal expansion, following the anisotropy in thermal
55 properties of the different constituting minerals (intergranular cracks). The second mechanism
56 is the development of micro- to macro-cracks within grains (intragranular cracks), when the
57 minerals undergo a phase transition, mechanically enhanced by the formation of cavities due
58 to rapid degassing or volume changes [8]. A quantitative estimation of the damage amount and
59 a precise knowledge of its evolution and influence on the mechanical properties of the rocks
60 exposed to heating has been only recently addressed.

61 In the last decades, few researches have been conducted for improving the knowledge on the
62 mechanical behaviour of rocks affected by temperature exposure. Different rock types have
63 been tested, among them granite [8-18], carbonatic rocks [19-24], salt [25] and sandstone [26-
64 28]. Generally, for rocks tested under their melting point, it has been observed that mechanical
65 and physical properties change significantly following temperature increase, demonstrating a
66 strong dependence on this parameter.

67 Even if the previous findings cannot be strictly generalized since the physical and mechanical
68 behaviours, after exposure to heating, depend on the specific mineral composition, grain size,
69 pre-existing crack damage of the chosen rocks, for all previous studies [8-28] two main trends
70 can be highlighted:

- 71 - In carbonatic rocks, salt and sandstone, for temperatures up to 200-300°C, mechanical
72 properties show a moderate increase of strength with temperature, due to dilatant effects
73 generated by thermal expansion, which result in ‘hardening’ of the bulk volume and
74 sealing of microcracks. This is mirrored by no clear increase in micro-cracks after
75 thermal treatment and consequent no evident changes in porosity and density. For
76 granite, this behaviour is shifted at temperature up to 500-600°C [29].
- 77 - Generally, for temperatures higher than 400-600°C, a significant thermal damage is
78 observed, with a progressive reduction of mechanical properties and an increase in
79 porosity. This has been related to an increase in crack density observed with
80 microscopic analyses. These effects are much more pronounced in carbonate rocks
81 where at temperatures between 560°C and 800°C decarbonization occurs [2, 30].

82 Among the available laboratory tests, the physical and mechanical properties of rocks exposed
83 to heating can be evaluated by either performing mechanical tests in controlled high-
84 temperature conditions reproducing in-situ thermal constraints [9-10, 25-26, 31], or carrying

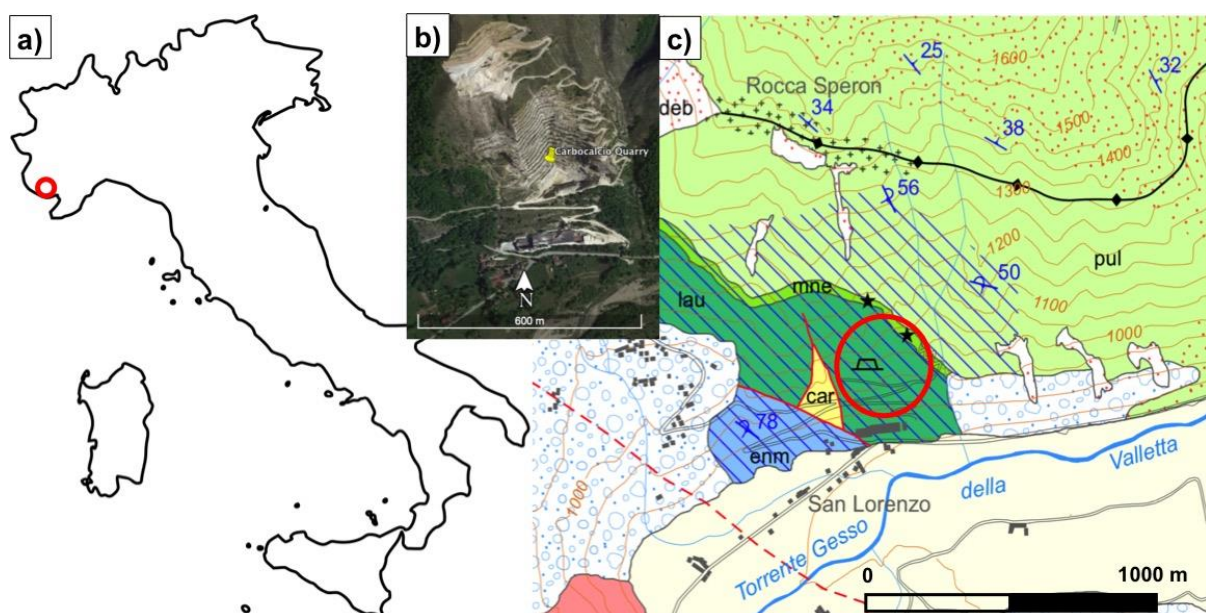
85 out comparative measurements before and after the thermal treatment (pre- and post-heating)
 86 [19]. If adequate confining pressure is applied with temperature, the first methods may allow
 87 for a simulation of specific site conditions at depth (i.e. volcanic edifices or geothermal
 88 reservoirs). Complex testing apparatus are however needed and sensors are usually limited in
 89 number and designed to operate away from the hottest zone, so that measurements may result
 90 inaccurate. The second test methodology, in which samples are firstly subjected to a thermal
 91 cycle and then tested at room temperature conditions, allow for a separated analysis of the
 92 effects of each treatment within a cycle of heating and cooling and can take advantage of a
 93 much denser array of sensors, thus significantly improving the reliability of the measurements.
 94 The purpose of this paper is to investigate the evolution of physical and mechanical properties
 95 of a marble rock type after different thermal treatments. Marble is natural stone extensively
 96 used during ancient times in many archaeological sites and nowadays it is still attractive for
 97 building purposes. Moreover, its worldwide diffusion makes it involved in many engineering
 98 applications such as geothermal energy extraction and deep drilling. In all these cases, it can
 99 be exposed to temperature gradient and consequently, the knowledge related to the evolution
 100 of its physical and mechanical features become fundamental. Porosity, ultrasonic pulse velocity
 101 (UPV), electrical resistivity (ER) and UCS were measured on core samples treated with thermal
 102 cycles from 105°C up to 600°C. Moreover, microscopic observations were performed on thin
 103 sections of cores subjected to the same thermal cycles. Correlations between destructive and
 104 non-destructive tests as a function of temperature were observed and deeply analysed also in
 105 correlation with the observed micro-cracking patterns.

106 2. Material and Methods

107 2.1 Description of rock samples and heating procedure

108 Tested samples were collected in the Carbocalcio quarry (Figure 1) in the North-Western
 109 Italian Alps (Valdieri Municipality, Southern Piedmont Region) where extremely pure calcium
 110 carbonate is extracted, treated and selected for sale as granulated and micronized. In this area,
 111 the outcrops belong to the Middle Jurassic–Lower Cretaceous Provençal succession placed at
 112 the North-Eastern side of the Argentera Massif (Figure 1c) in the Western Alps [32-33].

113



114

115 Figure 1: (a) Location, (b) satellite view and (c) geological sketch (after [30]) of the study area (red circle).
 116 Keys: enm: dark marls, calcareous marls and shales; lau: fine-grained limestones (lausa Limestone); mne: dark

117 shales and marls; pul: alternation of limestones and marly limestones; blue circle: glacial deposits; pale yellow:
 118 alluvial deposits; blue lines: Valdieri marble.

119

120 The main known characteristics of the tested rock type are listed in Table 1.

121 Table 1: Mean physical and mechanical characteristic and mineralogical composition of the studied marble.

Physical and mechanical characteristics	
Parameter	Mean value
Dry density [kg/m ³]	2720
Wet density [kg/m ³]	2740
Peak friction angle [°]	45
Residual friction angle [°]	39
Peak coesion [kPa]	96
Residual coesion [kPa]	75
Uniaxial Compressive Strenght [MPa]	115
Elastic modulus [GPa]	150
P-wave velocity [m/s]	7500
S-wave velocity [m/s]	4170
Dry apparent resistivity [Ohm m]	15800
Wet apparent resistivity [Ohm m]	12000
Porosity [-]	0.15
Mineralogical composition	
Calcite	99.90%
Quartz	>0.1%

122

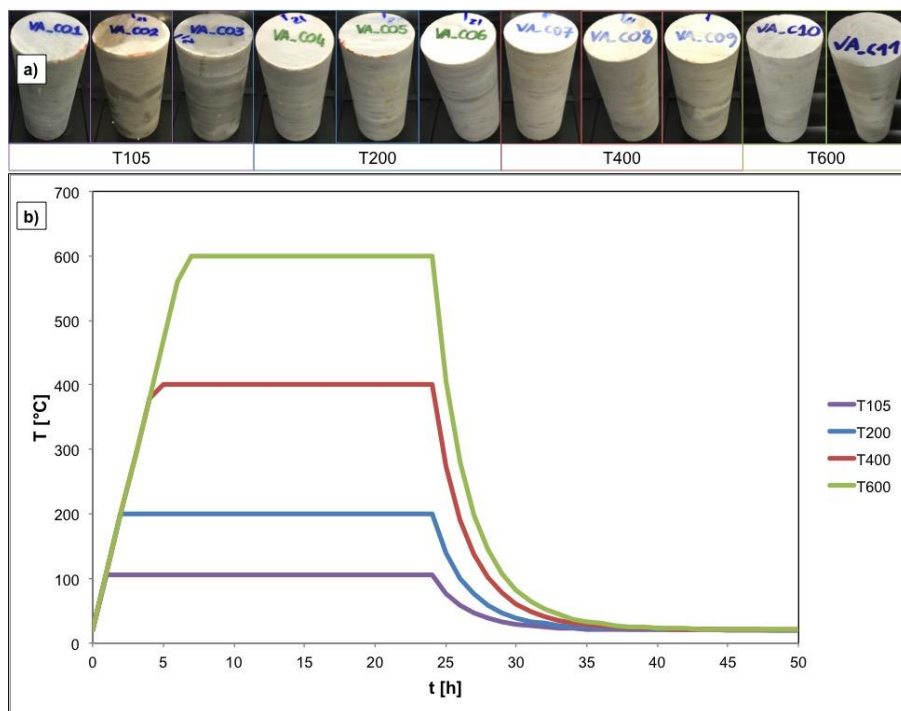
123 The carbonatic rock mass (Lausa limestone) consists in fine-grained limestone, with abundant
 124 decimeter-thick beds of polymictic breccias, generally clast-supported, with millimeter to
 125 decimeter sized clasts of mudstones, coarsely crystalline dolostones and finely crystalline
 126 dolostones. Lausa limestones are followed by grey mudstones and crinoid-rich wackestones,
 127 in centimeter to decimetre thick beds, with abundant silicified portions. Fault rocks
 128 (carnieules), extremely deformed dark-coloured schists and finely bedded grey marbles with
 129 dark-grey levels are also present near the extracted white marble.

130 Carbonates are locally affected by a diffuse hydrothermal dolomitization occurred in the Early
 131 Cretaceous, at a very shallow burial depth, and was related to the expulsion of hot fluids (about
 132 200°C) through faults and fractures during episodes of fault activity. Samples for this study
 133 collected within this carbonatic formation can be therefore considered as belonging to the
 134 Valdieri Marbles according to [3].

135 The mechanical and physical properties of eleven core specimens collected, with a diameter of
 136 50 mm and a length of 100 mm, were measured in the laboratory in natural and after-heating
 137 conditions. To ensure samples homogeneity and representativeness, the specimens were drilled
 138 from a single rock block with approximate dimensions of 0.8x0.5x0.4 m³.

139 A weak anisotropy parallel to bedding, due to a preferential orientation of microcrystalline
 140 calcite grains, has been observed for the block. This bedding has been confirmed on the tested
 141 block by several ultrasonic pulse velocity (UPV) measurements performed along three
 142 perpendicular directions of the block. Averaged UPVs measured parallel and perpendicular to
 143 the bedding were of 7500 m/s and 7000 m/s respectively, underling the weak anisotropy of the

144 studied rock. The cylindrical core drilling was performed perpendicular to this bedding. Most
 145 of the samples show indeed a weak horizontal layering (Figure 2a).
 146 The eleven specimens extracted from the block were grouped into four sets (Figure 2a). Each
 147 set was composed of three core samples (except one with only two specimens), in order to have
 148 a repeatability of the measurements, and was subjected to a comparable thermal treatment but
 149 reaching different target temperatures. Target temperatures of 105°C (T105), 200°C (T200),
 150 400°C (T400) and 600°C (T600) were reached for the different sets (Figure 2b). Each thermal
 151 cycle was composed of three stages (Figure 1b): firstly, the samples were heated in a furnace
 152 at a heating rate of 0.06°C/s. Secondly, once the target temperature was reached, the specimens
 153 were held in the furnace for 24 h. Finally, in order to avoid thermal shocks, the specimens were
 154 cooled down to room temperature in the furnace. Before and after the thermal treatment, all
 155 mechanical and physical properties were measured and later compared. Standard deviations of
 156 the measured and calculated parameters values have been also evaluated following the error
 157 propagation law.
 158



159
 160 Figure 2: (a) Picture of the different sets of the marble specimens after heating to different temperatures and (b)
 161 scheme of the thermal treatment cycles followed by each sample set.

162 2.2 Density and porosity determination

163 The measurement of physical properties such as density, ρ , and porosity, n , is a good index of
 164 the degree of damage induced in the rock specimens after thermal treatment [19,20].
 165 Since the tested specimens have a regular geometry and they are non-friable and coherent
 166 rocks, density and porosity were determined following the “Suggested methods for
 167 porosity/density determination using saturation and caliper techniques” of ISRM [34]. With
 168 this aim, the bulk volume, V , of each specimen was calculated from an average of several
 169 caliper readings along each dimension. The specimens were then saturated by water immersion
 170 and repeated shaking (for removing trapped air) for 24 h. The saturated-surface-dry mass, M_{sat} ,
 171 was then determined by drying the surface with a moistened cloth, taking care to remove only
 172 surface water, and weighting the samples. The grain mass, M_s , was evaluated after a drying
 173 process in oven, at constant temperature of 105°C for 24 h.

174 Porosity and density (in dry, ρ_{dry} , and saturated, ρ_{wet} , sample conditions) were obtained
175 following:

176

$$177 \quad \rho_{dry} = \frac{M_s}{V} \quad (1)$$

178

$$179 \quad \rho_{wet} = \frac{M_{sat}}{V} \quad (2)$$

180

$$181 \quad n = \frac{100V_v}{V} \% \quad (3)$$

182

183 where V_v is the void volume:

184

$$185 \quad V_v = \frac{M_{sat} - M_s}{\rho_w} \quad (4)$$

186 2.3 UPV measurements

187 UPV measurements were performed using an ultrasonic pulse generation and acquisition
188 system (Pundit Lab, Proceq). Two 54-kHz point-source (exponentially shaped) transmitter-
189 receiver (tx-rx) transducers were used for P-wave (V_P) measurements, along the axial direction
190 of each core sample. Cylindrical 250-kHz tx-rx probes were instead employed for S-wave (V_S)
191 determination, along the same core direction. Measurements were conducted following ASTM
192 D2845-08 standard requirements [35]. For each sample, 20 ultrasonic traces were recorded,
193 using a sampling frequency of 2 MHz. Manual picking of the first arrival times was performed.
194 Determination of the P- and S- wave ultrasonic velocity was then straightforward as the
195 longitudinal dimension of each sample was previously measured. The representative velocity
196 of each sample was chosen as the average of the 20 measurements.

197 From the V_P/V_S ratio and the determined density values, Young's, E , and shear, G , moduli and
198 Poisson's ratio, ν , were calculated for each specimen. These mechanical parameters refer to
199 low-strain conditions and will be compared with those obtained from the first deformation
200 phase of UCS tests.

201 2.4 ER measurements

202 ER measurements were carried out with an on-purpose built measuring quadrupole connected
203 to a Syscal-Pro (Iris instruments) acquisition system. The instrumentation consisted of a rubber
204 jacket with four steel electrodes (2-mm diameter and 40-mm length), disposed at the edges of
205 two perpendicular diameters of the core sample at half of its longitudinal length (Figure 3a).
206 Electrical measurements were performed with current injection between two subsequent
207 electrodes (A and B, in Figure 3b) and measuring the resulting electric potential difference
208 between the remaining couple of electrodes (M and N, in Figure 3b). The current and potential
209 electrodes were progressively reversed and rotated around the sample, for a total of 8 different
210 potential measurements.

211

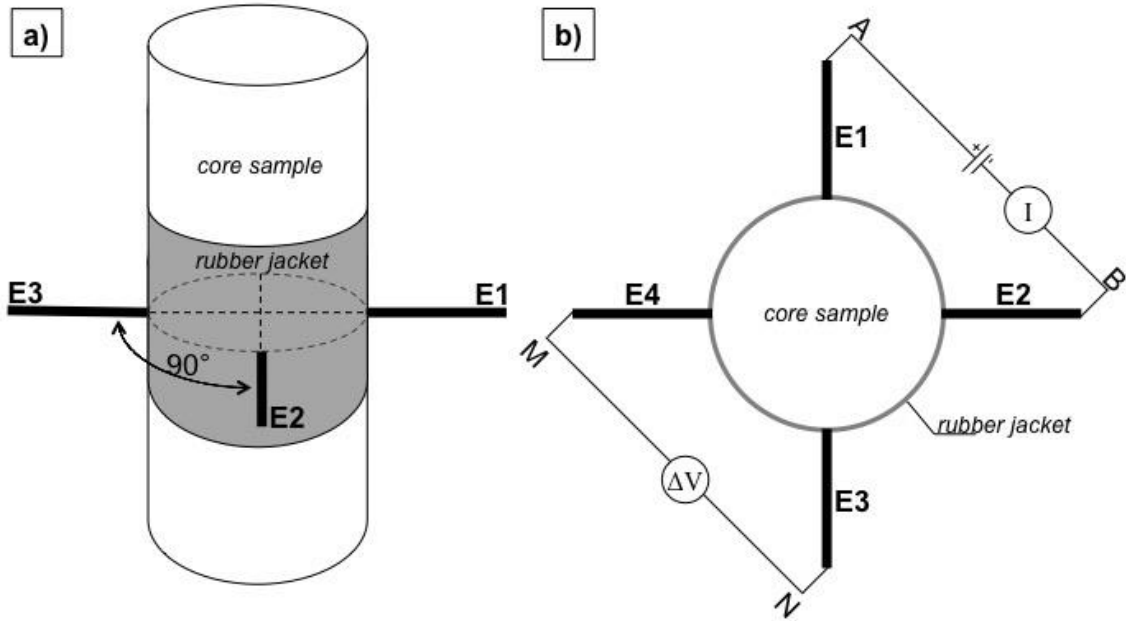


Figure 3: (a) Longitudinal view and (b) planar section of the electrical resistivity testing apparatus. E1 to E4: steel electrodes. A and B: current electrodes. M and N: potential electrodes.

The sequence was repeated three times on each sample, to obtain stable and repeatable results. From the ratio between the measured electric potential difference, ΔV_{MN} , and the injected current, I_{AB} , the determination of the sample apparent resistivity, ρ_a , follows:

$$\rho_a = k \frac{\Delta V_{MN}}{I_{AB}} \quad (5)$$

where k is a geometric factor, depending on the geometry of the adopted quadrupole. For the adopted array configuration, k was determined empirically by measuring the apparent resistivity of three water solutions ($\rho_{w1}=5 \Omega\text{m}$, $\rho_{w2}=10 \Omega\text{m}$, $\rho_{w3}=23 \Omega\text{m}$) in four plastic cylinders with variable diameter ($d_1=40 \text{ mm}$, $d_2=65 \text{ mm}$, $d_3=88 \text{ mm}$, $d_4=102 \text{ mm}$) with the described acquisition sequence. A constant diameter-normalized k value of:

$$k = 1.24\pi d \quad (6)$$

where d is the diameter of the sample, was found from the calibration procedure. This empirical determination is in agreement with the experiments and numerical simulations of [36]. The resulting 24 apparent resistivity measurements for each sample were averaged. Each sample was tested in both dry and saturated (wet) conditions. The saturated conditions were reached leaving the sample in a saline solution (with electrical conductivity equals to $1000 \mu\text{S}/\text{cm}$) for 24 h, with the aim of lowering the contact resistance between the electrodes and the sample surface and allowing for more stable measurements. This practice is universally recognized in ER measurements, particularly when rock materials are involved due to the high surface contact resistance (more than $1000 \Omega\text{m}$).

238 **2.5 UCS tests**

239 Mechanical properties were directly determined performing Uniaxial Compressive Strength
240 (UCS) tests. The tests were conducted using a MTS apparatus (MTS System Corporation)
241 equipped with a load cell of 250 kN, at a constant strain rate of 1 $\mu\text{m/s}$, following the
242 “Suggested methods for determining the Uniaxial Compressive Strength and Deformability of
243 Rock Materials” of ISRM [37]. Axial strain, ε_a , and diametric strain, ε_d , were measured using
244 electrical resistance strain gauges. The axial strain was defined as the mean value of the local
245 strains measured by two axial strain gauges, diametrically mounted along the specimen.
246 Uniaxial Compressive Strength, σ_u , Young’s modulus, E (tangent, E_t , average, E_{av} , and secant,
247 E_s), Poisson’s ratio, ν , and shear modulus, G , were evaluated for each specimen.

248 **2.6 Microscopic observations**

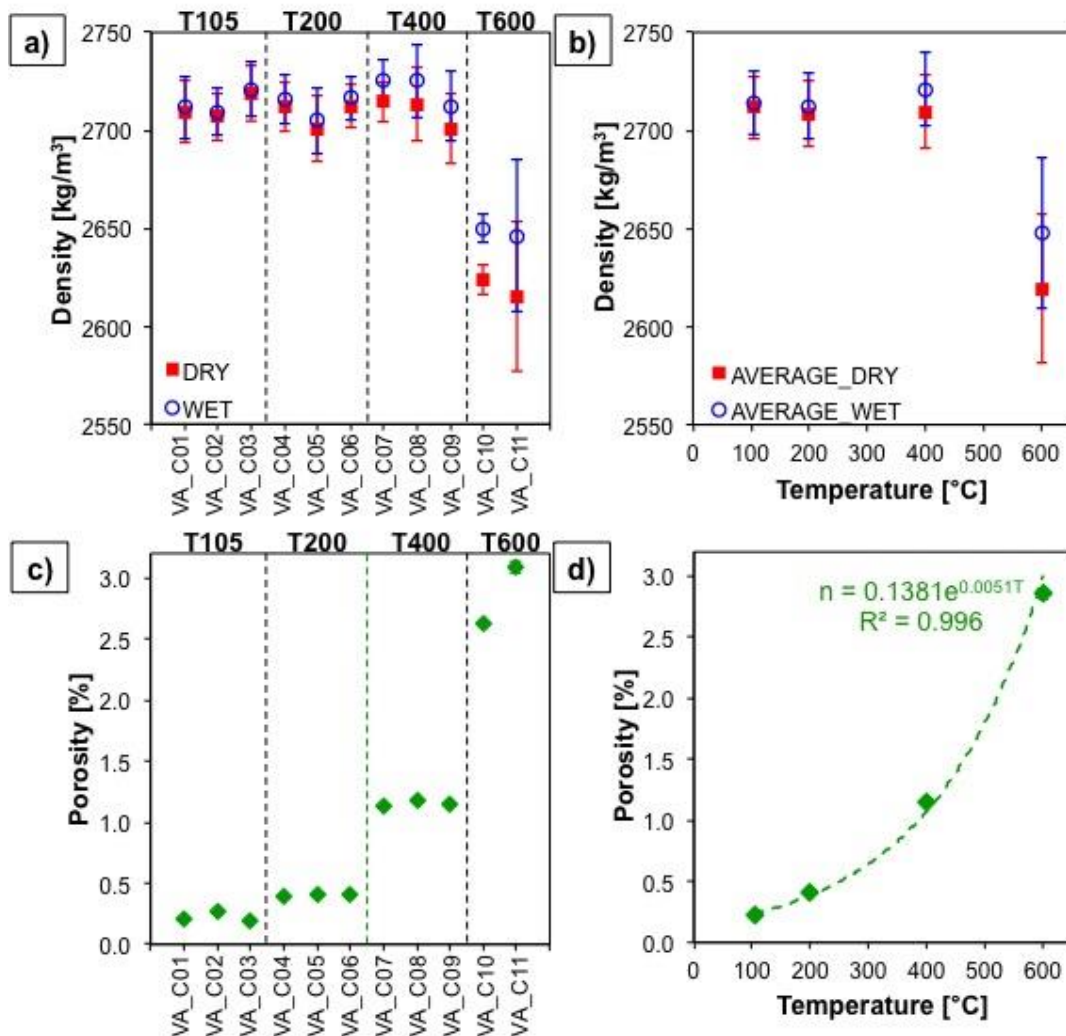
249 The microscopic effects of thermal treatment were observed using a transmitted polarized light
250 microscope. These analyses have the function of studying the widening and contraction of pre-
251 existing cracks and the development of new ones after thermal treatment.
252 Eight thin sections, two for each target temperature, were prepared: one perpendicular (\perp) and
253 one parallel (\parallel) to the sample bedding. These thin sections were not directly obtained from the
254 tested core samples (to avoid disturbances induced by destructive tests), but from additional
255 specimens subjected to the same thermal cycles, remaining from core resizing.
256

257 **3. Results and Discussion**

258 **3.1 Density and porosity determination**

259 Both density and porosity were evaluated firstly for each sample (Figures 4a and 4c) and then
 260 as an average over the samples subjected to the same thermal treatment (sample classes from
 261 T105 to T600, Figures 4b and 4d). Variations in density (dry, ρ_{dry} , and saturated (wet), ρ_{wet})
 262 and porosity, n , were observed, as shown in Figure 4. Analysing the results for each set of
 263 specimens (Figures 4a and 4c), low deviation from mean values has been observed: this aspect
 264 supports the hypothesis of homogeneity of material and it justifies the relative small number
 265 of specimens.

266 In general, the dry density of the specimens remains constant for temperature up to 400°C (with
 267 a slight increase at T = 400°C), after which it undergoes a significant decrease (red symbols in
 268 Figures 4a and 4b). The values of ρ_{wet} follow the same trend of ρ_{dry} , but showing a progressive
 269 divergence from dry values (blue symbols in Figure 4a and 4b).
 270



271 Figure 4: (a) Dry (red symbols) and wet (blue symbols) density evaluated for each sample. (b) Average dry (red
 272 symbols) and wet (blue symbols) density of each sample class (T105 to T600) as a function of the target
 273 temperature. (c) Porosity values for each sample after thermal treatment. (d) Relationship between the average
 274 porosity of each sample class and temperature. Where not visible, the dimensions of the error bars are lower
 275 than the marker size.
 276

277

278 This behaviour appears to be caused by the thermal expansion originated by the thermal
 279 treatment, which induces internal damage because of grain crushing and micro-crack formation
 280 and/or propagation that cause a rock pore volume increase and a density decrease. The presence
 281 of water is likely to act as an inhibiting factor, slightly reducing the brittle ongoing processes
 282 and thus determining slightly higher values. This hypothesis is confirmed by analysing sample
 283 porosity, graphed as a function of temperature (Figures 4c and 4d). After the thermal cycle,
 284 there is an increase in porosity that is moderate for temperatures up to 200°C and becomes
 285 more marked for higher temperatures. In the tested temperature range (from 105 to 600°C), the
 286 porosity rises from 0.2% to 3%, with a clear exponential increase after 200°C (porosity is still
 287 about 0.4% at this temperature) and a sharp increase after 400°C (from about 1% to 3%). This
 288 well agrees with the onset of calcite decomposition which occurs at around 560°C [30] and
 289 speeds up the micro-cracking mechanisms by phase transitions inducing rapid volume changes
 290 and extra void formations. By regression analysis, we obtain the characteristic exponential
 291 relationship from our experimental data by interpolating porosity and temperature, as follow:

$$292 \quad 293 \quad n = 0.1381e^{0.0051T} \quad (7)$$

294 where n is given in percentage. The goodness of this relationship is represented by the high
 295 value (0.996) of the coefficient of determination, R^2 .
 296

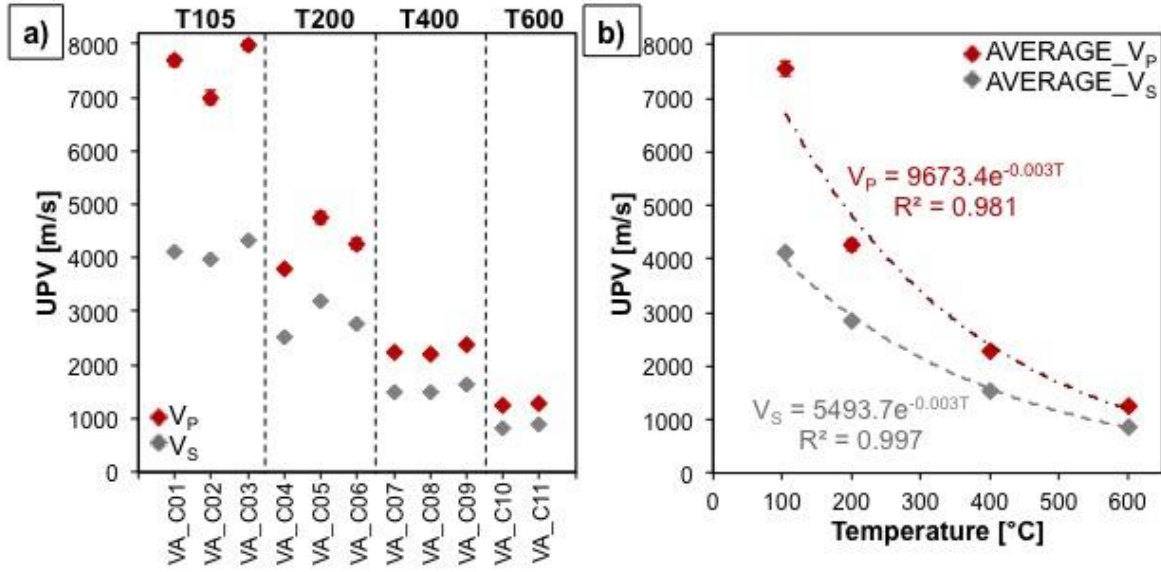
297 3.2 UPV measurements

298 A clear decrease in the UPV was found with increasing target temperature of the thermal
 299 treatment, as shown in Figure 5, both for P- and S-wave measurements. In general, samples
 300 treated at the same target temperature exhibited quite stable P- and S- wave velocity values
 301 (Figure 5a). The V_P/V_S ratio was found to reduce with increasing temperature. Two exponential
 302 relationships were fitted to the average velocities of each class (T105 to T600), following:

$$303 \quad 304 \quad V_P = 9673.4e^{-0.003T} \quad (8)$$

$$305 \quad 306 \quad V_S = 5493.7e^{-0.003T} \quad (9)$$

307 The two relationships (Figure 5b) show very high R^2 values, 0.981 and 0.997 respectively.
 308 These results are also in good agreement with the increase in porosity observed and the damage
 309 within the medium because of thermal cracking, which progressively slows the ultrasonic wave
 310 first arrival time at each step of temperature. In addition, since the V_P/V_S ratio is directly related
 311 to the sample Poisson's ratio, a clear change in the mechanical properties of the samples is
 312 expected with increasing temperature. Particularly, lower V_P/V_S ratios corresponds to lower
 313 Poisson's ratios. The reduced distance of the two curves in Figure 5b suggest therefore an
 314 exponential lowering of the Poisson's ratio of the material as a function of increasing
 315 temperature, mirroring the incremental damage due to cracks formation and eventually to
 316 calcite decomposition, which provides the lowest detected V_P/V_S ratios.
 317
 318



319 Figure 5: (a) P-wave (red symbols) and S-wave (light blue symbols) ultrasonic pulse velocities measured along
 320 the axial direction of each sample. (b) Relationships between the average P- and S-wave velocity of each sample
 321 class (T105 to T600) and the target temperature. Where not visible, the dimensions of the error bars are lower
 322 than the marker size.
 323

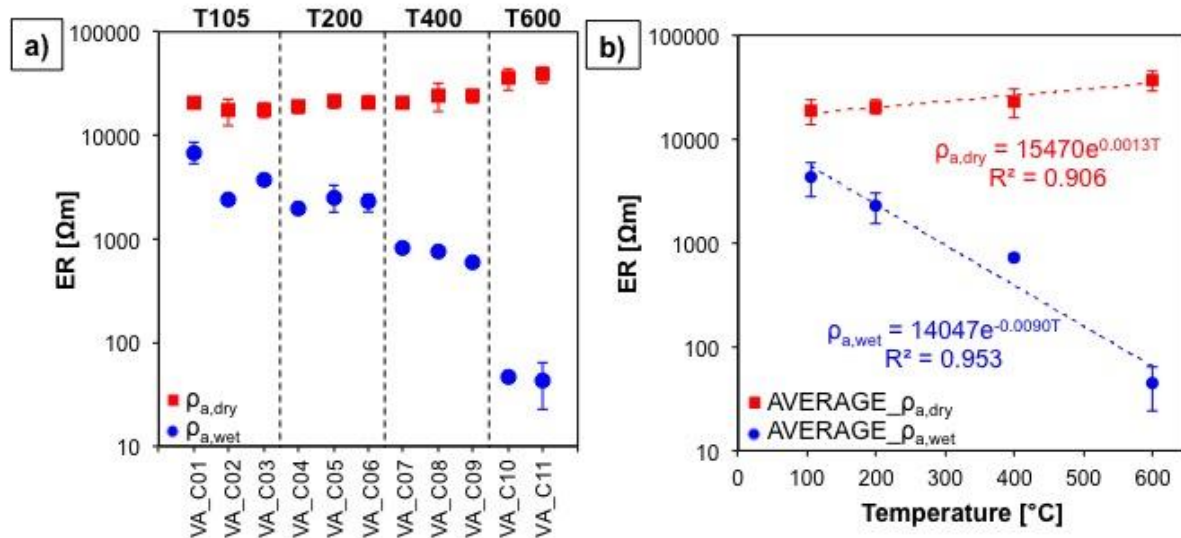
324 3.3 ER measurements

325 ER values measured on the same samples are summarized in Figure 6, both for dry ($\rho_{a,dry}$) and
 326 wet ($\rho_{a,wet}$) test conditions. As shown in Figure 6a, ER values are quite stable among the
 327 samples threatened to the same target temperature. Conversely, a clear modification in the
 328 electrical properties is found between the different classes. In particular, $\rho_{a,dry}$ values are found
 329 to slightly increase with increasing temperatures, while a clear decrease in $\rho_{a,wet}$ values is
 330 noticed. For electrical resistivity measured both in dry and wet conditions, the best fitting for
 331 the average values of the four classes is provided by exponential relationships (Figure 6b),
 332 following:

$$333 \rho_{a,dry} = 15470e^{0.0013T} \quad (10)$$

$$334 \rho_{a,wet} = 14047e^{-0.0090T} \quad (11)$$

335 Both relationships have very high R^2 values of 0.906 and 0.953 respectively.
 336
 337
 338
 339



340 Figure 6: (a) Dry (red symbols) and wet (blue symbols) electrical resistivity values measured on each sample.
 341 (b) Relationships between the average dry and wet average electrical resistivities of each sample class (T105 to
 342 T600) and the target temperature. Where not visible, the dimensions of the error bars are lower than the marker
 343 size.
 344

345
 346 The behaviour of the measured electrical properties with temperature is in agreement with the
 347 porosity and UPV measurements. In particular, the sample thermal cracking with increasing
 348 temperature generates an increase in the rock pore volume. These voids are filled by air (acting
 349 as an electrical insulator) in dry conditions. Accordingly, the measured $\rho_{a,dry}$ progressively
 350 increases. Conversely, in wet conditions pores and voids are filled by fluid (acting as an
 351 electrical conductor). These explanation is in accordance with the Sauer et al.' theory [38] that
 352 recognized three main paths which the electrical current can take in an unsaturated porous
 353 medium:

- 354 1 Through alternating layers of rock particles and interstitial soil solution
- 355 2 Through or along the surface of the rock particles in direct contact with one another
- 356 3 Through the interstitial fluid.

357 Consequently, if the porous medium is saturated by saline solution, the model 3 is dominant
 358 and the ER decrease with the increase of crack density. Vice-versa, in dry conditions, the
 359 volume void is filled by air, that has effectively zero conductance: the model 1 is dominant,
 360 ER moderately increase and it depends mainly by mineral shape and crack tortuosity.

361 In this configuration, $\rho_{a,wet}$ progressively reduces with increasing thermal damage, since the
 362 quantity of the fluid within the pore volume significantly increases. The very low values of
 363 $\rho_{a,wet}$ at 600°C are again consistent with the decomposition processes described above and the
 364 pervasive diffusion of fluids within the rock matrix, strongly increasing the conductivity.

365 3.4 UCS tests

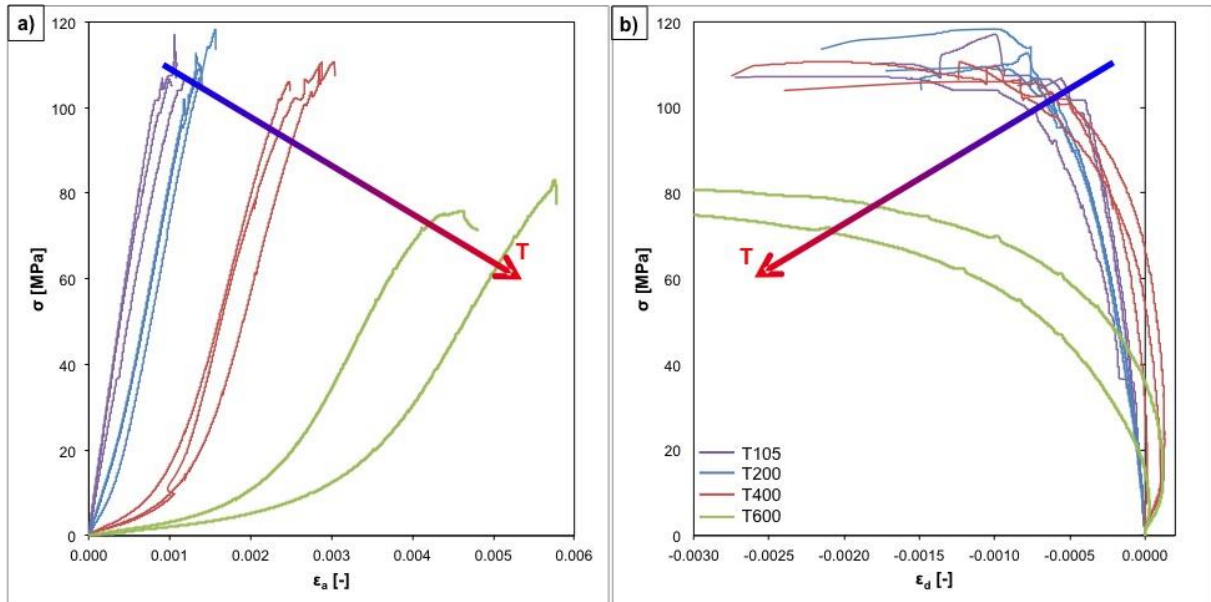
366 The results of UCS tests are listed in Table 2 and the complete stress-strain curves are shown
 367 in Figure 7. Results are also reported in Figure 8 as a function of the temperature treatment.
 368 The variations in σ_u are weak until a temperature of 400°C is attained (Figures 8a and 8b) with
 369 a slight increase (about 4 MPa on average) from 105 to 200°C . Then a significant drop in
 370 strength occurs from 400°C upwards that mirrors the major modifications going on within the
 371 microstructure because of mechanical softening due to incremental crack damage and approach
 372 to the calcite decomposition.
 373

374
375

Table 2: Summary of UCS test results for each sample (first column of σ_u , E_s , E_t , E_{av} , ν and G) and average for each sample class (second column of σ_u , E_s , E_t , E_{av} , ν and G).

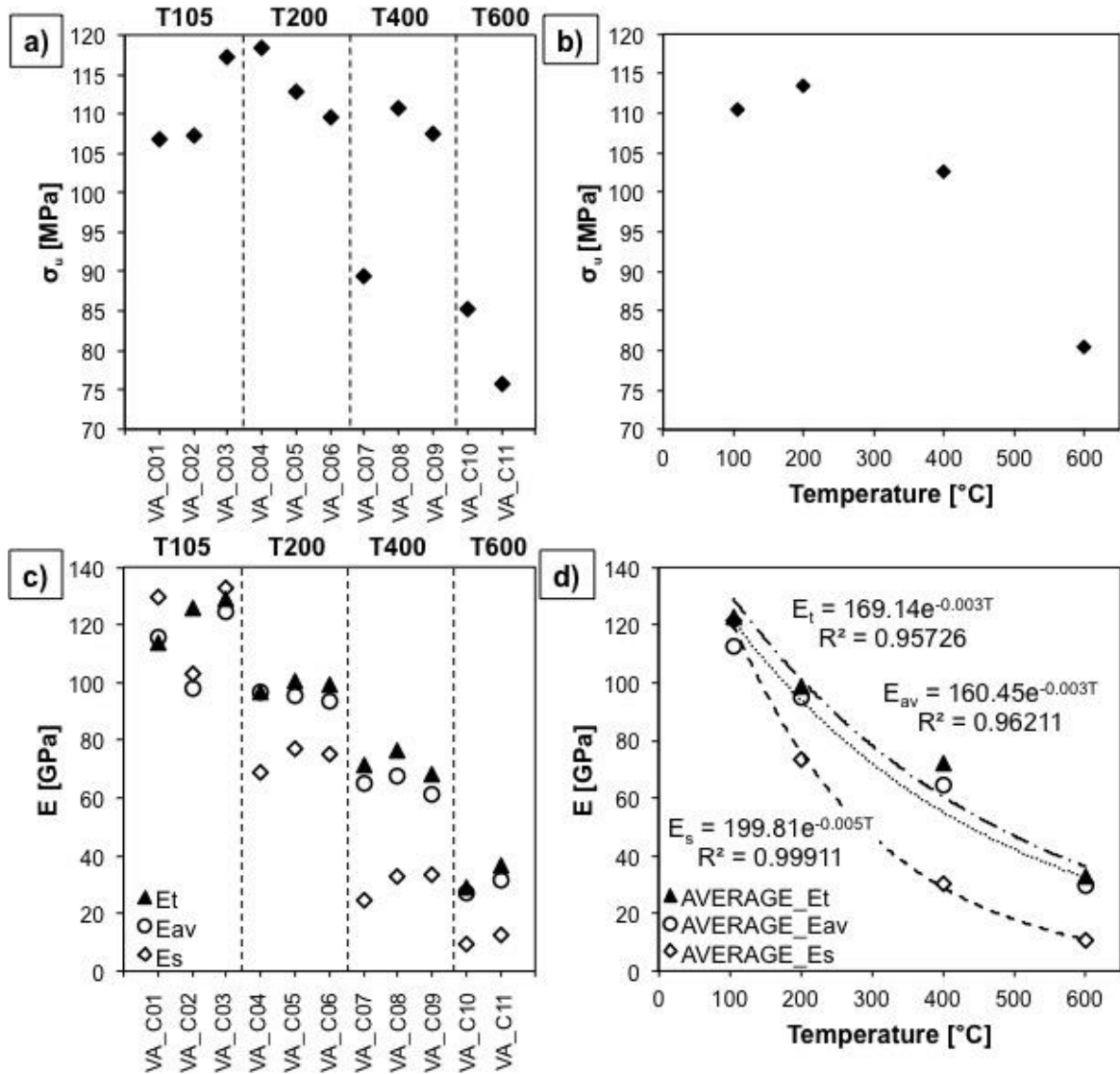
Thermal treatment	Sample	σ_u [MPa]		E_s [GPa]		E_t [GPa]		E_{av} [GPa]		ν		G [GPa]	
T105	VA_C01	107		129		114		115		0.38		47	
	VA_C02	107	110	103	122	126	123	98	113	0.43	0.39	36	44
	VA_C03	117		132		129		125		0.37		48	
T200	VA_C04	118		69		97		97		0.26		27	
	VA_C05	113	114	77	74	100	99	95	95	0.28	0.26	30	29
	VA_C06	110		75		99		94		0.22		31	
T400	VA_C07	89		24		71		65		-0.05		13	
	VA_C08	111	103	33	30	76	72	68	65	0.004	-0.003	16	15
	VA_C09	107		33		68		62		0.04		16	
T600	VA_C10	85	80	9	11	29	33	27	29	0.02	0.065	5	5
	VA_C11	76		12		37		31		0.11		6	

376
377



378
379
380

Figure 7: (a) Marble axial and (b) diametric stress-strain curves. The arrow represents the increase of heating temperature.



382 Figure 8: (a) UCS values measured on each sample. (b) Relationships between the average UCS of each sample
 383 class (T105 to T600) and the target temperature. (c) Tangent (triangles), average (circles) and secant (diamonds)
 384 Young's moduli for each sample after thermal treating. (d) Relationship between the average values of Young's
 385 moduli for each sample class and temperature.
 386

387 The Young's moduli (E_s, E_t and E_{av}) accordingly progressively decrease with respect to the
 388 temperature increase. As shown in Figure 8d, the drop in E_s is more significant compared to
 389 both E_t and E_{av}. Exponential relationships between elastic moduli and temperature were found:
 390

$$391 E_s = 199.81e^{-0.005T} \quad (12)$$

$$393 E_t = 169.14e^{-0.003T} \quad (13)$$

$$395 E_{av} = 160.45e^{-0.003T} \quad (14)$$

396 with R² of 0.999, 0.957 and 0.962 respectively.

397 The differences between the trend of E_s and E_t-E_{av} can be also explained by analysing the stress-
 398 strain curve in Figure 7a where it is clear how the non-linearity in the initial deformation phase
 399

400 increases as function of temperature. From 400°C target temperature, the samples also showed
401 a peculiar behaviour: the sign of diametric strain at the beginning of the tests was opposite to
402 the normal, indicating sample expansion and not sample contraction. This behaviour was
403 observed for each sample that belongs to T400 and T600 classes but is more marked for the
404 T600 class (see Figure 7b). This is an independent evidence of the major changes occurring
405 within the rock matrix bringing the sample to a more 'ductile' behaviour, which generates a
406 sample expansion compared to the contraction observed at lower temperatures driven from
407 elastic processes typical of the brittle behaviour. In order to verify that the anomalous sign in
408 diametric strain was neither an effect of surface, nor of the strain gauges, the UCS test on
409 sample VA_C08 was performed with an imposed diametric strain rate of -1 µm/s. For satisfying
410 this constrain, the sample was subjected to an instantaneous load of about 60 MPa, indicating
411 that up to that stress level sample expansion is still expected.
412 This effect results in negative or near zero average Poisson's ratios (see Table 2). The
413 progressive reduction of Poisson's ratio with temperature is coherent with what observed by
414 means of UPV measurements.

415 **3.5 Microscopic observations**

416 Photomicrographs of some thin sections treated at different temperature levels are shown in
417 Figure 9. Only thin sections perpendicular (\perp) to the sample bedding are shown as they better
418 display the damage developed within the samples, particularly in terms of crack damage.
419 In general all the reported images show the sample structure as constituted by a relatively
420 homogeneous grain size with finer-grained (up to 0.15 mm) isotropic and interlobate aggregate
421 of calcite. A weak preferred dimensional orientation of the slightly elongate crystals and
422 parallel clusters of coarser-grained crystals of calcite (up to 0.4 mm long) can also be observed.
423 These observations are coherent with the expected sample bedding.
424 From 400°C set temperature (Figure 9c), crack damages appear to be evident within this
425 general structure. Particularly, in Sample T600 (Figure 9d) sparse, but major fractures are
426 visible. These are oriented parallel to the sample anisotropy, and spatially associated with the
427 boundaries between the finer-grained matrix and the clusters of calcite. A clear weakness
428 fracture band is also evident in this sample.
429 These microscopic observations well indicate the progressive development of significant crack
430 damage within the samples from 400°C. A more marked increase in fractures is evident
431 particularly at 600 °C coherently with the calcite decomposition processes which enhance
432 fracture formation and propagation and in agreement with the measured reduction of
433 mechanical parameters within this range.
434

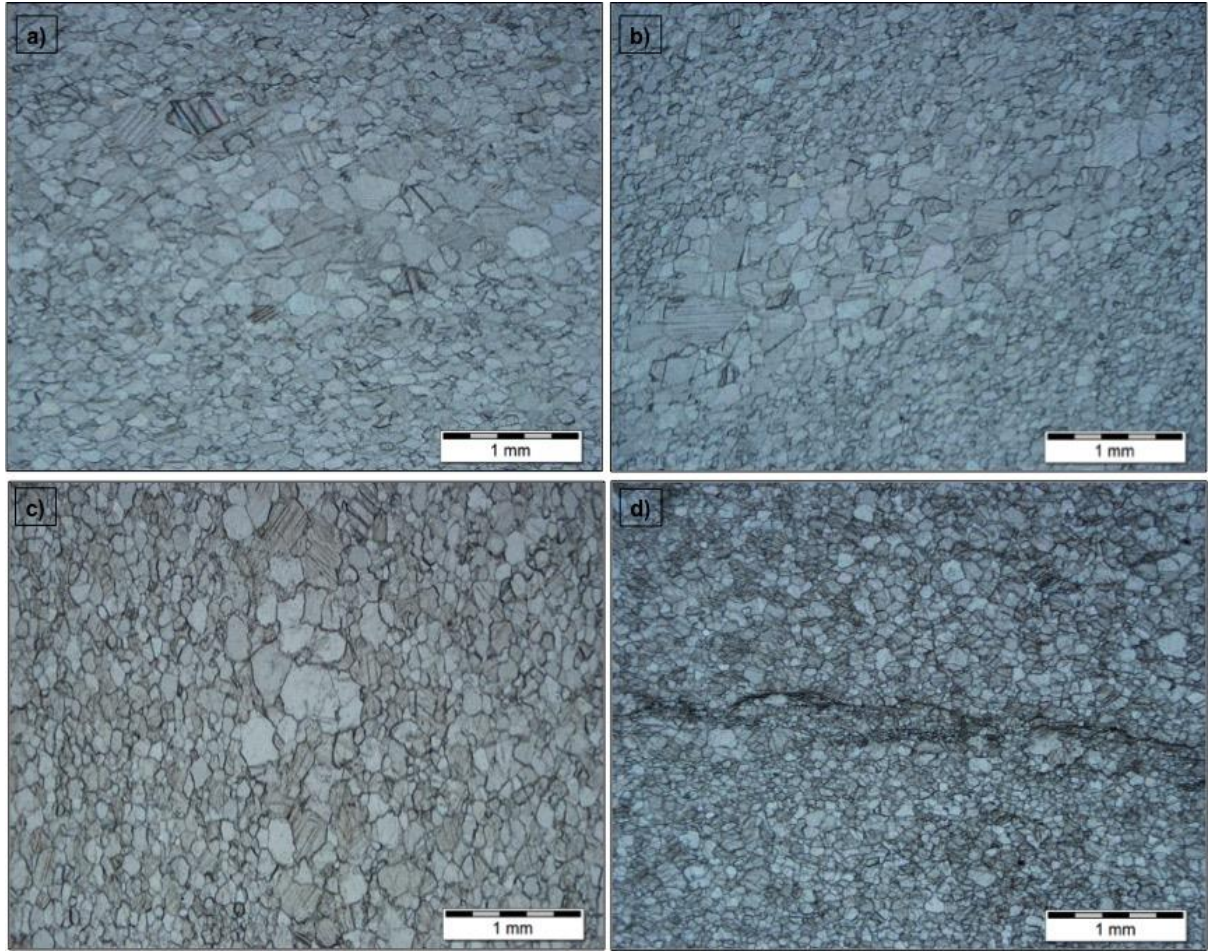


Figure 9. Photomicrograph of five thin sections at room temperature (a) and threated at 200°C (b), 400°C (c) and 600 °C (d). In (d), a clear crack was developed along the main anisotropy.

435
436
437

438 **4. Towards an Unified Damage Indicator**

439 This study has highlighted a degradation of the mechanical parameters with respect each step
440 of temperature applied and mirrored by all physical parameters measured. An exponential trend
441 is observed, driven specifically by the behaviour at temperatures above 400 °C, where thermo-
442 chemical reactions enhance significantly the crack damage formation and propagation
443 increasing the bulk porosity. Several authors have calculated exponential relationships between
444 physical parameters and temperature. For instance, Dwivedi et al. [9], in their study on salt
445 rocks, found an exponential relation between ultrasonic pulse velocity and temperature

446

$$447 \quad V_p = 3380e^{-0.0032T} \quad (15)$$

448

449 that is in good agreement with the one proposed here, especially regarding the exponential
450 value.

451 On the contrary, Liu et al. [39] performing post-high-temperature experiments on granite and
452 sandstone specimens proposed linear relationships between P-wave velocity and temperature
453 as follow

454

$$455 \quad V_{P,Granite} = 4700.167 - 4.608T \quad (16)$$

456

$$456 \quad V_{P,Sandstone} = 2018.988 - 1.569T \quad (17)$$

457

The same linear regression was found for Young's modulus

458

459

$$E_{Granite} = 37.092 - 32.160 \left(\frac{T}{1000} \right) \quad (18)$$

460

$$E_{Sandstone} = 21.262 - 14.210 \left(\frac{T}{1000} \right) \quad (19)$$

461

462 The authors [39] stated that physical and mechanical parameters after high-temperature
463 treatment all exhibit similar variation with temperature, showing a linear inverse dependence
464 for each parameter. Neglecting the interpolation law, in the present study the same behaviour
465 has been observed:

466 Zhao et al. [10], performing triaxial tests on coal and granite samples under high temperature
467 and high-pressure conditions, presented exponential relationships between Young's modulus
468 and temperature which show a similar trend to the one reported in this work and again very
469 similar exponential values.

470

$$E(\text{coal}) = 19.6e^{-0.005T} - 1.55 \quad (20)$$

472

$$E(\text{granite}) = 60e^{-0.006T} \quad (21)$$

473

474

475 These results were obtained at "in-situ" high temperature conditions and with limited
476 measurements of physical parameters. Thus the integrated methodology of several physical
477 and mechanical parameters "pre" and "post" thermal treatment described in this paper is a
478 reliable tool for studying the temperature effects due to multiple cycles of heating and their
479 effects on a variety of parameters.

480 In support of the findings reported in this paper, seismic velocities exponential relationships
481 are well recognized in literature [e.g. 40] between both V_P and V_S and porosity. These
482 relationships have the form:

483

$$V_{P,S} = V_{0 P,S} e^{-c n} \quad (22)$$

484

485

486 where V_0 is a reference velocity value, n is the porosity and c is a fitting parameter. The
487 reference velocity value is known to depend on the mineralogical composition of the sample
488 and is considered constant in geomaterials having the same composition. The fitting parameter
489 instead depends on the rock texture and can vary depending on the specific rock formation
490 process. In the presented experiments, it has been observed that the thermal effect is directly
491 correlated to the porosity (Figure 4d), which results to be the key parameter for analysing the
492 incremental damage induced by the thermal treatment. Moreover, these porosity relationships
493 are due to the increased crack density due to thermal degradation induced by the heating and
494 cooling stages. Particularly above 400 °C the inferred increase of crack density can be observed
495 by optical observations: Figure 9d shows the development of a pervasive system of fractures
496 along a weakness plane parallel to the principal anisotropy direction. Thermal expansion and
497 contraction along with decomposition processes can induce diffuse microcracking that
498 eventually localise along macro fractures that develop along the texturally favourable
499 orientations.

500 Since the porosity variation is intimately linked to the formation and propagation of fracture,
501 we can therefore use porosity as the most quantitative indicator of the thermally induced
502 damage, which we define as D_n . Based on Equation 7, it is possible to quantify D_n of the tested
503 specimens as follows:

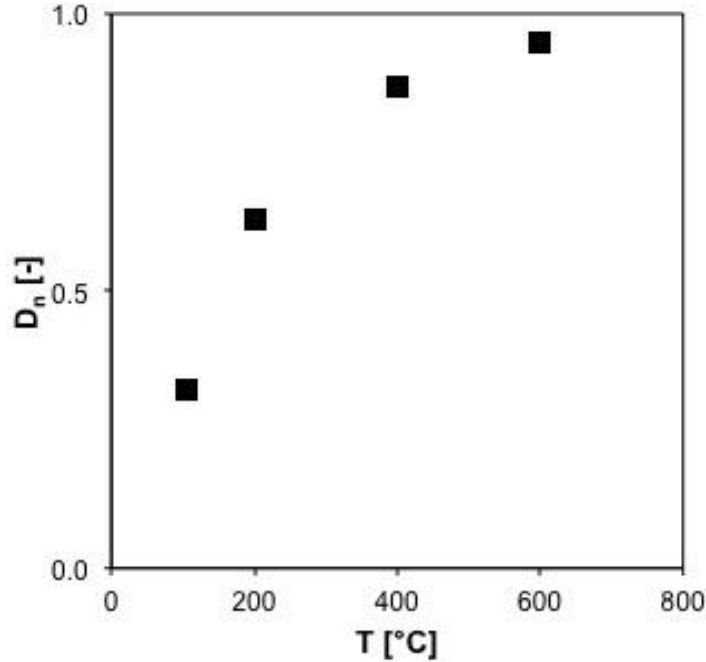
504

$$D_n = 1 - \frac{n_{RT}}{n(T)} \quad (23)$$

505

506
507
508
509
510
511
512

where n_{RT} is the room-temperature porosity and $n(T)$ is the porosity evaluated at the different target temperatures. D_n can assume values ranging from 0 to 1 (Figure 10): when it is 0 there are no effects of temperature on the sample porosity. Vice versa, when it is 1 the damage is so diffused that the rock loses cohesion. It should be noted that for the tested specimens, at 600 °C, the value of D_n is 0.94. Thus, the considered rock is close to total thermal damage.



513
514

Figure 10: Thermal damage, D_n , vs temperature.

515
516
517
518
519
520
521

Given that the observed thermal degradation effect on the rock samples is mainly driven by changes in porosity we therefore suggest that a formulation like equation 15 can exist relating the temperature and other physical properties, such as seismic velocities and electrical resistivity, for which the porosity influence result to be relevant. Determined empirical relationships with porosity, shown in Figure 11a and Figure 11b for UPV and electrical resistivity respectively, follow:

522

$$n = 76652V_p^{-1.439} \quad (24)$$

523

524

$$n = 174326V_s^{-1.631} \quad (25)$$

525

526

$$n = 0.08F^{-0.55} \quad (26)$$

527

528

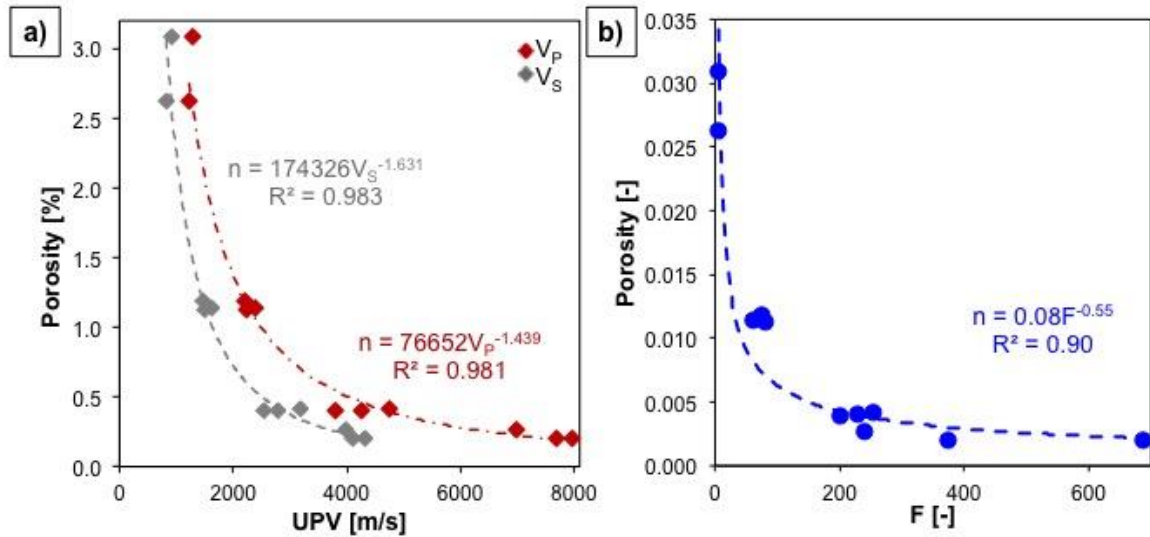
529

where F is the formation factor, expressed as the ratio between $\rho_{a,wet}$ and the fluid resistivity. These relationships have a very high R^2 , of 0.981, 0.983 and 0.90, confirming the strong dependence of the measured parameters on the rock porosity.

530

531

532



533 Figure 11: Empirical relationships for porosity estimation from (a) P- and S-wave ultrasonic pulse velocities, (b)
 534 wet electrical resistivity (measured on saturated samples).
 535

536
 537 Therefore the proposed thermal degradation relationship can assume the form:

$$538 \quad P(T) = P_0 A(T) \quad (27)$$

539
 540 where $P(T)$ is the considered physical parameter, P_0 its mineralogical reference value and $A(T)$
 541 is a function, dependent on temperature T . As previously shown, in scientific literature there
 542 are many relationships based on this model [9, 10, 39, 40]. The function $A(T)$ should comply
 543 with these requirements: firstly, P_0 should be constant in lithology with the same mineralogy
 544 and secondly, it should be convenient to assume that $A(T)$ tends to 1 when T is close to room
 545 temperature. Both prescriptions can be fulfilled if $A(T)$ follow an exponential law and
 546 consequently equation 27 can be rewritten as :

$$547 \quad P(T) = P_0 e^{-cT} \quad (28)$$

548
 549 where c is the fitting parameter dependent on the specific rock structure.

550
 551 In the present work we propose in equations 8 to 14 these two last calibrating factors for the
 552 tested rock. Similar calibration procedures could be undertaken for different rock types to allow
 553 for a precise quantification of the thermal degradation effect.

554
 555 Despite this well-defined behaviour on the measured physical parameters, σ_u is observed to
 556 follow a different trend. Indeed, a moderate increase of σ_u is observed till a certain temperature
 557 level. Analysing the stress-strain curves of Figure 7a, T200 specimens mark, for the tested
 558 marble, this turning point. Accordingly, to other authors [20-24], during UCS tests, due to crack
 559 closing and grain rearrangements there is a densification stage that, from one side increases the
 560 axial deformation (as expected) but on the other side increases the axial strength.

561
 562 UCS tests also showed other two interesting behaviours: the first one is the non-linearity in the
 563 initial deformation phase (Figure 7a) that is direct consequence of the anelasticity due to the
 564 increase of the amount of microcracks generated by thermal treatment in the specimens.

565
 566 The second is the negative value of Poisson's ratio for T400 and T600 specimens. For isotropic
 567 materials, the elasticity theory imposes that E shall be greater than 0 and ν varying between -1
 and 0.5. Thus, theoretically, negative values of ν are allowed. However, in experimental tests
 ν always results positive for real isotropic material.

568 The most plausible explanation for negative values of ν is the existence of residual stresses
 569 induced by the thermal cycles (presumably during cooling). The rise in temperature increases
 570 the crack density and lead to the weakening or even loss of grain boundary bonds, eventually
 571 producing unconsolidated material that under stress is mobilized plastically and flows along
 572 the sample.

573 The combined measurement of both P- and S-wave velocities offers the opportunity to retrieve
 574 low-deformation (initial deformation phase of strain-stress curve) mechanical parameters (E,
 575 G and ν) from indirect and non-destructive tests, following:

$$576 \quad G = \rho V_S^2 \quad (28)$$

$$577 \quad \nu = \frac{V_P^2 - 2V_S^2}{2(V_P^2 - V_S^2)} \quad (29)$$

$$580 \quad E = 2G(1 + \nu) \quad (30)$$

583 E, G and ν values from UCS tests were evaluated at an axial load of 10 MPa and considering
 584 the correspondent values of axial and diametric strain.

585 In Table 3, the results of the E, G and ν values estimated from UPVs and derived from UCS
 586 tests are listed. The general trend of the investigated parameters agrees with the previous
 587 observations: increasing the temperature, there is a drop in mechanical properties for both
 588 estimated and measured ones. The error in the estimation is quantifiable in less than 10% on
 589 average. The main differences concern the negative values of Poisson's ratio for the classes
 590 T400 and T600. Since V_P cannot be lower than V_S , Equation 21 can never return negative
 591 results.

592 Table 3: Comparison between low-deformation mechanical parameters (E, ν and G) evaluated from UCS tests
 593 and UPV measurements.
 594

Thermal treatment	Sample	E_{10MPa} [GPa]		E_{UPV} [GPa]		ν_{10MPa}		ν_{UPV}		G_{10MPa} [GPa]		G_{UPV} [GPa]	
T105	VA_C01	135		119		0.26		0.30		54	46		
	VA_C02	110	129	108	119	0.18	0.24	0.26	0.28	47	52	43	46
	VA_C03	143		131		0.28		0.29		56	51		
T200	VA_C04	36		38		0.07		0.10		17	17		
	VA_C05	60	51	60	48	0.10	0.10	0.09	0.11	27	23	27	22
	VA_C06	57		47		0.15		0.13		25	21		
T400	VA_C07	10		13		-0.09		0.10		5	6		
	VA_C08	11	11	13	14	-0.11	-0.07	0.08	0.09	6	6	6	6
	VA_C09	13		15		-0.01		0.08		6	7		
T600	VA_C10	4	4	4	4	-0.04	-0.03	0.09	0.05	2	2	2	2
	VA_C11	5		4		-0.01		0.01		3	2	2	2

595
 596

597 5. Conclusions

598 Temperature is a key parameter for modelling many geological engineering applications (deep
 599 drilling, geothermal energy exploitation, nuclear waste disposal, CO2 storage etc.) since it has

600 a significant influence on physical and mechanical properties of rocks. However, since each
601 rock type has a different behaviour after thermal treatment, it is important to develop dedicated
602 studies and calibrated equations for each lithology.

603 In this paper, a series of laboratory tests on an Italian marble was performed for investigating
604 the variation of the rock physical behaviour as a function of temperature. Several parameters
605 (ρ , n , V_P and V_S , ρ_a , σ_u) were measured on core samples subjected to four different target
606 temperatures (105, 200, 400 and 600°C). Microscopic observations on thin sections were
607 analyzed to evaluate the heating/cooling effects on marble microstructures.

608 For the analysed rock, the range of temperatures from 200 to 400°C marks a turning point in
609 the trend of physical and mechanical characteristics: up to 200°C, all the considered parameters
610 are not significantly sensitive to the temperature. Indeed, the axial strength shows a moderate
611 increase (about 4 MPa) despite the axial deformation increases. This behaviour might be
612 associated with compaction due to the closure of intergranular cracking that are not completely
613 linked. Even if this aspect is not so evident by analysing thin sections due to some limitations
614 in their preparation procedure, this hypothesis can be supported by analysing the trend of F
615 values. At 400°C, there is a significant drop in ρ , V_P and V_S , F , σ_u and E values and an increase
616 in n . The presence of intragranular cracks and the high intergranular crack density are the
617 leading parameters of this degradation.

618 The previous observations suggest that n can be considered the most sensitive parameter with
619 temperature. Thus, the authors proposed the coefficient D_n for measuring the thermal damage
620 of rocks. If D_n is close to 0, it means that the effects of temperature on the rock sample can be
621 neglected; vice-versa, if it is close to 1, the sample has undergone irreversible degradation.

622 Finally, it is important to underline the exponential dependence of physical and mechanical
623 parameters with temperature for the studied marble rock. This dependence was already
624 observed in other works for other rock types [9, 10, 26]. Future works should be done for
625 verifying this trend.

626 A remark must be made on the size of the sample to be representative: since macroscopically
627 and microscopically the tested marble doesn't show a relevant heterogeneity (as also confirmed
628 by the low variability in the measurements between samples of the same group), the authors
629 considered the number of specimens sufficient for providing reliable and representative results.
630 However, this aspect shall be taken into account if other lithologies will be considered in future
631 works.

632 Since in many geo-engineering applications the temperature is coupled with pressure, it will
633 be interesting to investigate the effects of the latter on rock characteristics, especially if the
634 proposed relationships are applicable or they should be modified.

635 Another aspect that will require further analyses is the observation of negative Poisson's ratio
636 at high temperature: in particular it will be interesting to investigate the reasons of this
637 behaviour and if it occurs in other lithotypes.

638 **Conflicts of Interest**

639 The authors declare that there is no conflict of interest regarding the publication of this paper.

640 **Acknowledgements**

641 Special acknowledgements should be given to Carbocalcio Cuneese S.p.A that agrees the use
642 of its materials for observation, sampling and laboratory tests.

643 Funding Statement

644 This project has received funding from the European Union's Horizon 2020 research and
645 innovation programme under the grant agreement No. 727550.

646 References

- 647 [1] Homand-Etienne F and Houpert R. Thermally induced microcracking in granites: characterization and
648 analysis. *Int. J. Rock. Mech. Min. Sci. & Geomech. Abstr.* 1989;26;2:125-134.
- 649 [2] Castagna A, Ougier-Simonin A, Benson PM et al. Thermal Damage and Pore Pressure Effects on
650 Brittle-Ductile Transition of Comiso Limestone. *Journal of Geophysical Research – Solid Earth*, in
651 press.
- 652 [3] Gomez-Heras M, McCabe S, Smith, Bernard BJ, Fort R. Impacts of Fire on Stone-Built Heritage An
653 Overview. *Journal of Architectural Conservation.* 2009;15:47-58.
654 doi:10.1080/13556207.2009.10785047.
- 655 [4] Giuliani A and Fornaro M. Criteri geologico applicativi per il reperimento di materiali lapidei originari
656 per il restauro della Cappella della SS. Sindone (Torino, NW Italia). *VIII Convegno Nazionale dei*
657 *Giovani Ricercatori di Geologia Applicata.* 2010:86-89.
- 658 [5] Koca MY, Ozden G, Yavuz AB et al. Changes in the engineering properties of marble in fire-exposed
659 columns. *Int. J. Rock Mech. Min. Sci.* 2006;43:520–530.
- 660 [6] Yavuz AB, Topal T. Thermal and salt crystallization effects on marble deterioration: Examples from
661 Western Anatolia, Turkey. *Eng. Geo.* 2007;90:30-40.
- 662 [7] Rutter EH. The influence of temperature, strain rate and interstitial water in the experimental
663 deformation of calcite rocks. *Tectonophysics.* 1974;22:311-334.
- 664 [8] Jansen DP, Carlson SR, Young RP, Hutchins DA. Ultrasonic-imaging and acoustic-emission
665 monitoring of thermally-induced microcracks in lac-du-bonnet-granite. *J. of Geophys. Res. Sol. Earth.*
666 1993;98:22231-22243.
- 667 [9] Dwivedi RD, Goel RK, Prasad VVR, Sinha A. Thermo-mechanical properties of Indian and other
668 granites. *Int. J. Rock Mech. Min. Sci.* 2008;45;3:303-315.
- 669 [10] Zhao Y, Wan Z, Feng Z, Yang D, Zhang Y, Qu F. Triaxial compression system for rock testing under
670 high temperature and high pressure. *Int. J. Rock Mech. Min. Sci.*, vol. 52, pp. 132-138, 2012.
- 671 [11] Tullis J and Yund RA. Experimental deformation of dry Westerly granite. *J. Geophys. Res.*
672 1977;82:5705-5718.
- 673 [12] Wong TF. Effects of temperature and pressure on failure and post-failure behavior of Westerly granite.
674 *Mech. Mater.* 1982;1:3-17.
- 675 [13] David C, Menéndez C, Darot M. Influence of stress-induced and thermal cracking on physical
676 properties and microstructure of La Peyratte granite. *Int. J. Rock. Mech. Min. Sci.* 1999;36;4:433-448.
- 677 [14] Chaki S, Takarli M, Agbodjan WP. Influence of thermal damage on physical properties of a granite
678 rock: porosity, permeability and ultrasonic wave evolutions. *Constr. Build. Mater.* 2008;22;7:1456–
679 1461.
- 680 [15] Chen YL, Ni J, Shao W, Azzam R. Experimental study on the influence of temperature on the
681 mechanical properties of granite under uni-axial compression and fatigue loading. *Int. J. Rock. Mech.*
682 *Min. Sci.* 2012;56;8:62-66.
- 683 [16] Liu S and Xu J. Mechanical properties of Qinling biotite granite after high temperature treatment. *Int.*
684 *J. Rock. Mech. Min. Sci.* 2014;71:188-193.
- 685 [17] Yin T, Li X, Cao W et al. Effects of Thermal Treatment on Tensile Strength of Laurentian Granite
686 Using Brazilian Test. *Rock. Mech. Rock Eng.* 2015;48:2213-2223.
- 687 [18] Chen YL, Wang SR, Ni J, Azzam R, Fernández-steeger TM. An experimental study of the mechanical
688 properties of granite after high temperature exposure based on mineral characteristics. *Eng. Geol.*
689 2017;220:234-242.
- 690 [19] Peng J, Rong G, Cai M, Yao MD, Zhou CB. Physical and mechanical behaviours of a thermal-
691 damaged coarse marble under uniaxial compression. *Eng. Geol.* 2016;200:88-93.
- 692 [20] Ferrero AM and Marini P. Experimental Studies on the mechanical behaviour of two thermal cracked
693 marbles. *Rock Mech. Rock Eng.* 2000;34;1:57-66.
- 694 [21] Lion M, Skoczylas F, Ledésert B. Effects of heating on the hydraulic and poroelastic properties of
695 bourgogne limestone. *Int. J. Rock. Mech. Min. Sci.* 2005;42;4:508-520.

- 696 [22] Malaga-Starzec K, Åkesson U, Lindqvist JE, Schouenborg B. Microscopic and macroscopic
697 characterization of the porosity of marble as a function of temperature and impregnation. *Constr. Build.*
698 *Mater.* 2006.
- 699 [23] Yavuz H, Dermirdag S, Caran S. Thermal effect on the physical properties of carbonate rocks. *Int. J.*
700 *Rock. Mech. Min. Sci.* 2010;1:94-103.
- 701 [24] Gonzalez-Gomez WS, Quintana P, May-Pat A, Avilés F, May-Crespo J, Alvarado-Gil JJ. Thermal
702 effects on the physical properties of limestones from the Yucatan Peninsula. *Int. J. Rock Mech. Min.*
703 *Sci.* 2015;75:182-189.
- 704 [25] Liang WG, Xu SG, Zhao YS. Experimental study of temperature effects on physical and mechanical
705 characteristics of salt rock. *Rock Mech. Rock Eng.* 2006;39:5:469-482.
- 706 [26] Ranjith PG, Viete DR, Chen BJ, Perera MSA. Transformation plasticity and the effect of temperature
707 on the mechanical behaviour of Hawkesbury sandstone at atmospheric pressure. *Eng. Geol.*
708 2012;151:120-127.
- 709 [27] Ding QL, Ju F, Mao XB, Ma D, Yu BY, Song SB. Experimental investigation of the mechanical
710 behaviour in unloading conditions of sandstone after high-temperature treatment. *Rock Mech. Rock*
711 *Eng.* 2016;49:7:2641-2653.
- 712 [28] Sun Q, Chen S, Gao Q, Zhang W, Geng J, Zhang Y. Analyses of the factors influencing sandstone
713 thermal conductivity. *Acta Geodyn. Geomater.*, vol. 2, no. 186, pp. 172–180, 2017.
- 714 [29] Brotóns V, Tomás R, Ivorra S, Alarcón JC. Temperature influence on the physical and mechanical
715 properties of a porous rock: San Julian's calcarenite. *Eng. Geol.* 2013;167:117-127.
- 716 [30] Bakker R, Violay M, Benson P, Vinciguerra S. Ductile flow in sub-volcanic carbonate basement as the
717 main control for edifice stability: New experimental insights. *Earth and Planetary Science Letters.*
718 2015; 430:533-541.
- 719 [31] IMAGE-D3.03. Physical properties of rock at reservoir conditions. Integrated Methods for Advanced
720 Geothermal Exploration. Collaborative Project – GA No. 608553. 2016:1-70.
- 721 [32] Carraro F, Dal Piaz GV, Franceschetti B, Malaroda R, Sturani C, Zanella E. Note illustrative della
722 Carta Geologica del Massiccio dell'Argentera alla scala 1:50.000. *Memorie della Società Geologica*
723 *Italiana.* 1970;9:557–663 (in Italian).
- 724 [33] Barale L, Bertok C, d'Atri A, Martire L, Piana F, Domini G. Geology of the Entracque–Colle di Tenda
725 area (Maritime Alps, NW Italy). *Journal of Maps.* 2016;12;2:359-370.
- 726 [34] ISRM. Suggested methods for determining water content, porosity, density, absorption and related
727 properties and swelling and slake-durability index properties. 1977.
- 728 [35] ASTM D2845-08. Standard Test Method for Laboratory Determination of Pulse Velocities and
729 Ultrasonic Elastic Constants of Rock,” ASTM, International (American Society for Testing and
730 Materials), West Conshohocken, Pennsylvania, USA. 2008.
- 731 [36] Clement R, Bergeron M, Moreau S. COMSOL Multiphysics modelling for measurement device of
732 electrical resistivity in laboratory test cell. *Proceedings of the 2011 COMSOL Conference in Stuttgart.*
733 2011.
- 734 [37] ISRM. Suggested methods for determining the uniaxial compressive strength and deformability of rock
735 materials. 1977.
- 736 [38] Sauer MCJr, Southwick PE, Spiegler KS, Wyllie MRJ. Electrical conductance of porous plugs: Ion
737 exchange resin-solution system. *Ind. Eng. Chem.* 1955;47:2187-2193.
- 738 [39] Liu S, Xu J. An experimental study on the physico-mechanical properties of two post-high-temperature
739 rocks. *Eng. Geo.* 2015;185:63–70.
- 740 [40] Musso G, Cosentini RM, Foti S, Comina C, Capasso G. Assessment of the structural representativeness
741 of sample data sets for the mechanical characterization of deep formations. *Geophysics*, 2015;80:441-
742 457.